A daily basin-wide sea ice thickness retrieval methodology: Stefan's Law Integrated Conducted Energy (SLICE)

James Anheuser[1], Yinghui Liu[2], and Jeffrey R. Key[2]

[1]AOS UW-Madison, Madison, Wisconsin
[2]Center for Satellite Applications and Research, NOAA/NESDIS, Madison, Wisconsin

Correspondence: James Anheuser (anheuser@wisc.edu)

Abstract. As changes to Earth's polar climate accelerate, the need for robust, long–term sea ice thickness observation datasets for monitoring those changes and for verification of global climate models is clear. By coupling a recently developed algorithm for retrieving snow–ice interface temperature from passive microwave satellite data to a thermodynamic sea ice energy balance relation known as Stefan's Law, we have developed a new retrieval method for estimating thermodynamic sea ice thickness growth from space: Stefan's Law Integrated Conducted Energy (SLICE). The advantages of the SLICE retrieval method include

5 daily basin-wide coverage and a potential for use beginning in 1987. The method requires an initial condition at the beginning of the sea ice growth season in order to produce absolute sea ice thickness and cannot as yet capture dynamic sea ice thickness changes. Validation of the method against ten ice mass balance buoys using the ice mass balance buoy thickness as the initial condition show a mean correlation of 0.991 and a mean bias of 0.008 m over the course of an entire sea ice growth season.

10 Estimated Arctic basin-wide sea ice thickness from SLICE for the sea ice growth seasons beginning between 2012 through 2019 capture a mean of 12.0% less volumetric growth than a CryoSat-2 and Soil Moisture and Ocean Salinity (SMOS) merged sea ice thickness product (CS2SMOS) and a mean of 8.3% more volumetric growth than the Pan-Arctic Ice–Ocean Modeling and Assimilation System (PIOMAS). The spatial distribution of the sea ice thickness differences between the retrieval results and those reference datasets show patterns consistent with expected sea ice thickness changes due to dynamic effects. This new

15 retrieval method is a viable basis for a long–term sea ice thickness climatology, especially if dynamic effects can be captured through inclusion of an ice motion dataset.

1 Introduction

Observing sea ice concentration and areal extent from satellites is a well established practice (Liu et al., 2016; Meier et al., 2017; Markus and Cavalieri, 2000; Markus and Cavalieri, 2009; Comiso, 2009; Lavergne et al., 2019). There are methods

20 based on data in the visual, infrared and microwave wavelength bands and climate data records produced from these methods are commonly cited as polar climate indicators (Stroeve et al., 2012; Screen and Simmonds, 2010; Liu et al., 2009).

While sea ice concentration is more readily observed, sea ice thickness provides a more complete characterization of the state of the climate system because it allows for calculation of sea ice volume and latent heat release. Recent literature has made clear that reliable long-term observations of basin wide sea ice thickness are needed in order to constrain the representations of

25 sea ice in global climate models (Mayer et al., 2019). Sea ice thickness based observations of sea ice volume can be used along with other observations to refine the large range of projected sea ice area and volume across coupled global climate models (Docquier and Koenigk, 2021). Indeed, the lack of reliable long term sea ice thickness observation constraints is the primary barrier to reducing the uncertainty in future sea ice area and volume projections (Massonnet et al., 2018).

Sea ice thickness derived from space-based altimetry data collected by satellites like CryoSat-2 and IceSat-2 stand as the
30 current state of the art but are limited in spatial coverage and temporal resolution (Connor et al., 2009; Kwok and Cunningham, 2008; Markus et al., 2017, Wingham et al., 2006; Laxon et al., 2013). Other strategies for retrieving sea ice thickness include the use of a one-dimensional surface energy balance model driven by satellite products (Key et al., 2016) and the use of low-frequency passive microwave satellite data for estimating the thickness of thin sea ice (Mecklenburg et al., 2012). Assimilating available observational data into a global coupled ocean sea ice model is also effective (Zhang and Rothrock, 2003). A newer
35 approach involves correlating sea ice thickness with sea ice age (Liu et al., 2020). The various available products are discussed and compared against one another both qualitatively and quantitatively in Wang et al. (2016) and against upward looking sonar (ULS) in Sallila et al. (2019).

Recent efforts to retrieve temperature at the boundary between snow and sea ice, referred to as the snow–ice interface temperature, have opened a new door in polar climate observation (Lee and Sohn, 2015; Lee et al., 2018; Kilic et al., 2019). These
40 methods take advantage of radiances from the Advanced Microwave Scanning Radiometer (AMSR)-Earth Observing System (-E), AMSR2, the Special Sensor for Microwave Imager (SSM/I) and Special Sensor Microwave Imager/Sounder (SSMIS) passive microwave instruments using channels whose wavelengths are not significantly absorbed by snow and therefore carry information from the snow–ice interface. Kang et al. (2021) demonstrated the utility of these snow–ice interface temperature data by using them to nudge a sea ice model, improving the model's results. By coupling this newly available snow–ice inter-
45 face temperature data with Stefan's Law governing the thermodynamics of sea ice growth (Stefan, 1891; Lepparanta, 1993), we introduce a promising new method of estimating sea ice thickness called Stefan's Law Integrated Conducted Energy (SLICE).

As sea ice accretes on the underside of the ice layer, the latent heat of fusion conducts up through the ice to the snow–ice interface. In Stefan's Law, that conducted heat and therefore rate of accretion is calculated using a heat conduction equation with the snow–ice interface temperature as the upper boundary condition and the local freezing temperature of sea water set
50 as the lower boundary condition (Stefan, 1891; Lepparanta, 1993). By using the satellite retrieved snow–ice interface in this relationship and with an initial thickness condition in hand, SLICE is able to retrieve daily rate of ice accretion and sea ice thickness on a basin-wide scale during the sea ice growth season. With the required passive microwave observations available from 1987 to current, there is potential for a sea ice thickness time series of the same span.

2 Data

55 The SLICE retrieval method described here utilizes passive microwave brightness temperatures and a passive microwave based sea ice concentration dataset. A preliminary validation of the retrieval method references sea ice thickness from ice mass balance buoy data, satellite radar altimeter data and a sea ice thickness model reanalysis.

2.1 Snow–Ice Interface Temperature

Outgoing longwave radiation on the low frequency end of the microwave spectrum is not significantly absorbed by snow on
the Earth's surface (Mathew et al., 2009). Previous efforts to take advantage of this fact to measure the temperature of sea ice
have relied on infrared (IR) measurements or models to augment the results (Comiso, 1983; Hall et al., 2004; Hewison and
English, 1999). This process leads to errors and IR data is only available in clear sky conditions. In Lee and Sohn (2015), only
microwave brightness temperatures are used. The method uses the horizontal and vertical polarity 6.9 GHz channel brightness
temperatures from the passive microwave AMSR-E or AMSR2 instruments along with a combined Fresnel relationship (Sohn
and Lee, 2013) to determine the local microwave emissivity of sea ice. This emissivity along with the observed brightness
temperatures yields the snow–ice interface temperature. We have replicated the procedure from Lee and Sohn (2015) for use
in the retrieval method described here.

Assuming the absorption by snow and the atmosphere is negligible, the snow–ice interface temperature can be related to
satellite observed brightness temperature from a channel with a weighting function peak at the snow ice interface through

$$T_H(\nu) = \epsilon_H(\nu)T_{si} \tag{1}$$

where $T_H(\nu)$ is satellite observed horizontally polarized spectral brightness temperature, $\epsilon_H(\nu)$ is local snow–ice interface
spectral emissivity for horizontal polarized emission and T_{si} is snow–ice interface temperature. This relationship also holds
for vertically polarized satellite observed spectral brightness temperature and spectral emissivity $T_V(\nu)$ and $\epsilon_V(\nu)$. As such,
the following relationship also holds:

$$\frac{\epsilon_H(\nu)}{\epsilon_V(\nu)} = \frac{1 - r_H(\nu)}{1 - r_V(\nu)} = \frac{T_H(\nu)}{T_V(\nu)} \tag{2}$$

where $r_H(\nu)$ and $r_V(\nu)$ are horizontal and vertical spectral reflectance, respectively. A combined Fresnel relationship closes
Equation 2 and allows solving for one of the emissivities (Sohn and Lee, 2013):

$$r_V(\nu) = \left(r_H(\nu)^2 \frac{1 + r_H(\nu)^{-1/2}\cos 2\theta}{1 + r_H(\nu)^{1/2}\cos 2\theta} \right)^2 \tag{3}$$

where θ is satellite viewing angle. The resultant emissivity can be inserted into Equation 1 to solve for T_{si}. Additional detail
can be found in Lee and Sohn (2015).

The AMSR-E and AMSR2 6.9 GHz channels were used to calculate snow–ice interface temperature here as in Lee and Sohn
(2015). The resultant snow–ice interface temperatures were found to require a bias correction of 5 K in order to match buoy
snow–ice interface temperatures and in order to produce the best sea ice thickness retrieval method results. This bias correction
may address atmospheric absorption and snow absorption to the extent that they cannot be assumed negligible. Figure 1 shows
snow–ice interface temperatures on 1 January 2013 calculated from AMSR2 radiances.

The AMSR-E and AMSR2 brightness temperatures available from the National Snow and Ice Data Center (NSIDC) were
used in this study (https://nsidc.org/data/AE_SI25/versions/3; https://nsidc.org/data/AU_SI25/versions/1; Cavalieri et al., 2014;
Markus et al., 2018). The AMSR-E data is available for June 2002 through October 2011 and the AMSR2 data is available for
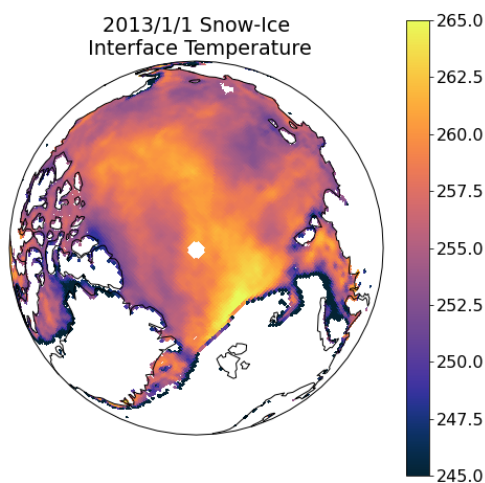
Figure 1. Snow–ice interface temperatures on 1 January 2013 derived from AMSR2 radiances.

July 2012 to the present. The AMSR2 data has been intercalibrated with the AMSR-E data and the brightness temperatures
90 between these two instruments are treated here as a continuous dataset (Markus et al., 2018). The data is provided on a 25 km
polar stereographic grid but when needed on a basin-wide scale for use with the sea ice thickness retrieval method described
here, the data were linearly interpolated to a 25 km Equal-Area Scalable Earth (EASE) 2.0 grid. In Lee et al. (2018), the method
is adapted for use with the SSM/I 19.35 GHz channel to allow for retrieval of snow–ice interface temperature beginning in 1987.

Liquid water at the emitting layer in the form of open ocean or melt ponds interferes with the snow–ice interface temperature
95 algorithm (Lee and Sohn, 2015). As such and in line with Lee and Sohn (2015), the snow–ice interface is only calculated here
in grid cells with greater than 95% sea ice concentration. A method for calculating snow–ice interface temperature for grid
cells with under 95% sea ice concentration is described in the appendix of Lee and Sohn (2015) but is not implemented here
pending further investigation. The snow–ice interface temperature retrieval is also subject to the polar data gap associated with
AMSR-E/2 data. For basin-wide analysis, the polar data gap is filled using two-dimensional linear interpolation.

100 ## 2.2 Ice Mass Balance Buoys

In order to statistically characterize the sea ice thickness retrieval method described herein, ice mass balance buoy data served
as the reference. The ice mass balance buoys were deployed and maintained by the United States Army Corps of Engineers
Cold Regions Research and Engineering Laboratory (CRREL) (Perovich et al., 2021). Undeformed ice floes are chosen for
buoy sites to ensure the buoy is representative of the surrounding ice (Polashenski et al., 2011).

105   Of particular relevance to comparison with the retrieval method described here, a buoy is a Lagrangian observation as it travels with the ice pack rather than remaining geospatially stationary. The retrieval method calculates ice thickness change and requires Lagrangian tracking of ice thickness making buoy data a good match for validation.

Data fields used from the buoys were sea ice thickness and geolocation in latitude and longitude. Ice thickness is observed using two acoustic rangefinder sounders, one positioned above and one positioned below the ice. Each sounder has an accuracy

110   of 0.005 m (Richter-Menge et al., 2006). An Argos antenna mounted on the buoy transmits the geolocation and other observations at minimum twice per day (Richter-Menge et al., 2006). For this study, all data fields were resampled to 1 d resolution by calculating daily mean values. All buoys from the years 2003 to 2016 showing an entire season of sea ice thickness growth were used for comparison with the exception of buoys installed in landfast ice and those that show obvious dynamic effects. Table 1 provides relevant details pertaining to the buoys used. Buoy 2013F spanned two winter seasons and as such has been

115   divided into two buoy numbers, 2013F and 2013Fb, with 2013Fb covering the second winter season during which the buoy was deployed. As such, a deployment date is not listed for 2013Fb.

Table 1. A listing of United States Army Corps of Engineers Cold Regions Research and Engineering Laboratory (CRREL) Ice Mass Balance buoys used in this work. All buoys from 2003 to 2016 containing a full season of sea ice thickness growth are included, excluding those in landfast ice or showing obvious dynamic effects.

Buoy	Region	Ice Type	Deployment date
2003C	Beaufort Sea	Multi-year	2002/8/31
2005F	Central Arctic	Multi-year	2005/9/3
2006C	Beaufort Sea	Multi-year	2006/9/4
2012G	Central Arctic	First year	2012/10/1
2012H	Beaufort Sea	First year	2012/9/10
2012L	Beaufort Sea	Multi-year	2012/8/27
2013F	Beaufort Sea	Multi-year	2013/8/25
2013G	Beaufort Sea	Multi-year	2013/9/4
2013Fb	Beaufort Sea	Multi-year	-
2015F	Central Arctic	Multi-year	2015/8/13

Efforts to compare satellite based records of sea ice thickness with ground truth are hampered by the scale of the question. Ground truth measurements of sea ice are necessarily taken from a single point while satellites observe sea ice thickness on the scale of kilometers. The variability of sea ice across those kilometers leads to uncertainty in the comparison. It has been shown,

120   however, that while variability in absolute ice thickness may be significant on the scale of a satellite observation, sea ice growth and melt is relatively uniform on the satellite length scale (Polashenski et al., 2011). Therefore, while absolute comparisons of sea ice thickness between a ground truth and satellite observation may be tenuous, comparisons of growth over a winter season between single point ground truth and satellite based observations are more robust.

2.3 AWI CS2SMOS

125 CryoSat-2 is a currently operational radar altimeter (Wingham et al., 2006; Laxon et al., 2013) launched by the European Space Agency (ESA) in 2010. Similar to other satellite altimeters, ice thickness is determined from CryoSat-2 data by first calculating the thickness of the sea ice above sea level—known as the freeboard—and then assuming a snow loading and hydrostatic balance to determine sea ice mass which in turn is converted to thickness using an assumed density (Laxon et al., 2013). Gridded ice thickness products derived from ESA CryoSat-2 Level 1b data are provided by the ESA Centre for Polar Observation and

130 Modelling (CPOM) (Tilling et al., 2018), the National Aeronautics and Space Agency (NASA) Goddard Space Flight Center (GSFC) (Kurtz et al., 2014), the Alfred Wegener Institute (Ricker et al., 2014; Hendricks and Ricker, 2020; Ricker et al., 2017a), the NASA Jet Propulsion Laboratory (Kwok and Cunningham, 2015), the ESA Climate Change Initiative (Hendricks et al., 2018) and the Laboratoire d'Études en Géophysique et Océanographie Spatiales Center for Topographic studies of the Ocean and Hydrosphere (Guerreiro et al., 2017). The primary differences between these datasets relate to averaging period,

135 grid sizing and radar response waveform retracking.

The ESA Soil Moisture and Ocean Salinity (SMOS) satellite carries the Microwave Imaging Radiometer using Aperture Synthesis (MIRAS) instrument which measures 1.4 GHz passive microwave brightness temperatures at 35 to 50+ km resolution (Mecklenburg et al., 2012). While originally intended for measuring soil moisture and ocean salinity, the high penetration depth of the 1.4 GHz channel into sea ice allows for retrieval of an ice temperature that when incorporated into a radiative transfer

140 model yields a sea ice thickness estimate (Tian-Kunze et al., 2014). This approach has associated uncertainties in sea ice below 0.5 m thick that are lower than those of satellite altimeters.

Sea ice thickness observations from SMOS and CryoSat-2 have complimenting uncertainties. SMOS has high uncertainties when measuring thick ice and CryoSat-2 has high uncertainties when measuring thin ice (Ricker et al., 2017b). This creates an opportunity for synergy between the instruments. The AWI CS2SMOS dataset takes advantage of this synergy. By combining

145 the datasets through a weighted averaging scheme, root mean squared errors are reduced from 76 cm with CryoSat-2 alone to 66 cm and the squared correlation coefficient is increased from 0.47 with CryoSat-2 to 0.61 when compared against NASA Operation Ice Bridge data (Ricker et al., 2017b). The AWI CS2SMOS dataset is available at a weekly time resolution and on a 25 km EASE-Grid 2.0 and was used with the method demonstrated here due to the high spatial coverage.

2.4 PIOMAS

150 The Pan-Arctic Ice–Ocean Modeling and Assimilation System (PIOMAS) is a numerical model reanalysis product that couples the Parallel Ocean Program (POP) model developed at Los Alamos National Laboratory with a thickness and enthalpy distribution (TED) model (Zhang and Rothrock, 2003). The TED model includes a viscous–plastic sea ice rheology (Hibler, 1979) and a sea ice thickness distribution scheme that accounts for redistribution due to ridging (Thorndike et al., 1975). The model is driven by daily surface forcing and sea surface temperatures (SSTs) provided by National Centers for Environmental

155 Protection (NCEP)/ National Center for Atmospheric Research (NCAR) and NSIDC sea ice concentration in order to produce daily sea ice thickness data from 1978 to present (Schweiger et al., 2011).

2.5 AMSR SIC

The NASA Team 2 algorithm is a passive microwave brightness temperature based sea ice concentration algorithm (Markus and Cavalieri, 2000). It as an enhancement to the original NASA Team algorithm (Cavalieri et al., 1984; Gloersen and Cavalieri, 1986) in that it adds 85 GHz frequency brightness temperatures to the original algorithm, which used only 19 GHz and 37 GHz data, in order to better account for interference from surface effects. The algorithm utilizes open ocean and 100% ice concentration tie points in polarization ratio and spectral gradient ratios to determine sea ice concentration. While originally developed for use with SSM/I data (Markus and Cavalieri, 2000), the algorithm was planned to be and is now in use with AMSR-E and AMSR2 data. Here we use this AMSR-E and AMSR2 sea ice concentration data which is available from the NSIDC as a part of the same dataset that contains the brightness temperatures used to calculate snow–ice interface temperature (https://nsidc.org/data/AE_SI25/versions/3; https://nsidc.org/data/AU_SI25/versions/1; Cavalieri et al., 2014; Markus et al., 2018).

3 Methodology

Sea ice grows thicker through two primary physical mechanisms: thermodynamic phase change and dynamic changes due to the relative motion of the ice pack. The governing equation for sea ice thickness can be written as

$$\frac{\partial H}{\partial t} = f(t, H, \mathbf{x}) - \nabla \cdot (\mathbf{u}H) \tag{4}$$

where H is plane slab sea ice thickness, t is time, f is a function of time, thickness and position vector $\mathbf{x}$ describing thermodynamic sea ice thickness increase and $\mathbf{u}$ is the ice motion vector. This equation is analogous to Equation 3 in (Thorndike et al., 1975), but does not include the redistribution term in that equation because here we use a plane slab thickness H rather than a thickness distribution. The second term on the right hand side of Equation 4 captures dynamic thickness changes. The focus in the remainder of this section will be on the first term on the right hand side of Equation 4.

By coupling the conductive heat equation to a latent heat of freezing term, Stefan's Law relates the rate of thermodynamic sea ice thickness increase to the temperature difference between the snow–ice interface and bottom of the ice layer, the later of which is at or very near to the freezing temperature of sea ice (Stefan, 1891; Lepparanta, 1993). The physical explanation for this relationship is that the latent heat of freezing at the bottom of the ice is conducted up to and through the snow–ice interface. When the snow–ice interface temperature drops below the temperature at the bottom of the ice, heat provided by the latent heat of freezing is pulled to the snow–ice interface. In the method described here, a new satellite observation of snow–ice interface temperature (Lee and Sohn, 2015) drives the analytical solution to the Stefan's Law relationship in order to determine sea ice thickness growth.

Just as fluid flows across a pressure difference and electricity flows across a voltage difference, all heat transfer occurs across a temperature difference. Conduction is the transfer of heat across a solid medium and is always accompanied by a temperature difference across that medium. The equation governing one dimensional, steady state conduction is

$$\dot{q} = -\kappa (T_2 - T_1) / D \tag{5}$$

where $\dot{q}$ is heat per unit area or heat flux, κ is the thermal conductivity of the medium, T_1 and T_2 are the boundary temperatures
190 and D is the distance between the boundaries.

A change in the phase of a material must either release or accept energy as the molecular bonds and motion within the
material change. In the case of a phase change from liquid to solid, energy is released as the molecular motion is reduced with
the introduction of molecular bonds. The equation describing the one dimensional, latent heat release in this scenario is

$$\dot{q} = \rho_s L \frac{dD}{dt} \tag{6}$$

195 where $\dot{q}$ is heat per unit area or heat flux, ρ_s is the density of the solid phase of the material, L is the latent heat of fusion and
$\frac{dD}{dt}$ is the one dimensional change in solid material size per unit time.

In Stefan's Law, Equations 5 and 6 are combined via the common heat flux term, $\dot{q}$ to form

$$\frac{\partial H}{\partial t} = \frac{\kappa_i}{\rho_i L H} \left(T_f - T_{si} \right) \tag{7}$$

where ρ_i is the density of sea ice, L is the latent heat of fusion of sea ice, $\frac{\partial H}{\partial t}$ is the change in sea ice thickness per unit time, κ_i
200 is the thermal conductivity of sea ice, T_f is the freezing point of sea water, T_{si} is the snow–ice interface temperature and H is
sea ice thickness (Lepparanta, 1993). There are a number of assumptions inherent to this relationship (Lepparanta, 1993). First,
heat conduction in the horizontal direction is assumed to be negligible. Second, it is assumed that there is no thermal inertia
present in the ice. This means that the local derivative of temperature with respect to sea ice depth is constant throughout the
sea ice layer and the system is in equilibrium. The spatial derivative of temperature found in a typical heat equation reduces
205 to the temperature difference between the snow–ice interface temperature and the freezing point of water due to these first two
assumptions. Next, it is assumed that there is no internal heat source, such as the absorption of short wave radiation. This is
valid during polar winter and times of the year when solar incidence angles are very shallow. Last, heat flux from the sea water
to the sea ice is assumed negligible. A more detailed mathematical development of Stefan's Law than the following can be
found in Lepparanta (1993).

210 Equation 7 defines the thermodynamic growth function, f, found in Equation 4 and is equivalent to Equation 4 when dynamic
growth is neglected. Equation 7 is a differential equation with the following analytical solution (Lepparanta, 1993)

$$H^2 = H_0^2 + a^2 S \tag{8}$$

where a is defined as

$$a = \sqrt{\frac{2\kappa_i}{\rho_i L}}, \tag{9}$$

215 H_0 is the initial sea ice thickness and S is the sum of negative degree-days and is defined as

$$S = \int_0^t [T_f - T_{si}(\tau)] d\tau. \tag{10}$$

The time interval t chosen for the results shown herein is one day based on the daily availability of snow–ice interface tem-
perature. The value for a is taken to be 3.3 cm $(°\text{C}^{-1} \text{ d}^{-1})^{1/2}$ (Lepparanta, 1993). This equates to a density of 900 kg m^{-2},

a latent heat of fusion of 3.35 x 10^5 J kg^{-1} and a thermal conductivity of 1.9 W m^{-1} K^{-1}. The freezing point of sea water is
220 taken to be -2 °C.

At each time step, the sea ice thickness after thermodynamic growth is determined by solving Equation (4) for H given
an H_0 using the snow–ice interface temperature calculated at the nearest AMSR-E or AMSR2 grid cell. Because both H and
H_0 are squared in Equation (4) while the other terms are not, the change in sea ice thickness at each time step is dependent
on initial sea ice thickness. This necessitates this retrieval method be applied in a Lagrangian sense as the sea ice thickness
225 must be tracked and stored in order to accurately calculate the change at the next time step. Fortunately, this mathematical
characteristic also means this method is self correcting. In equation (4), thicker sea ice grows slower than thinner sea ice and
thinner sea ice grows faster than thicker ice with a given snow–ice interface temperature. This means sea ice that is too thick or
too thin will correct towards the true thickness. This relationship replicates the phenomenon described in Bitz and Roe (2004),
whereby thick ice grows slower than thin ice and vice versa.

230 **4 Results**

The SLICE sea ice thickness retrieval methodology can be applied on a single one-dimensional profile basis or across a large
area. Here we present results comparing one-dimensional profiles to ice mass balance buoy thicknesses and Arctic basin-wide
results compared to AWI CS2SMOS and PIOMAS data.

4.1 One-dimensional Profiles

235 The SLICE retrieval method results were compared to sea ice thickness from ice mass balance buoys. The retrieval method
was initialized with the buoy observed sea ice thickness on the day when the 14 d rolling average sea ice growth exceeded
1 mm d^{-1}. From this time step forward, the retrieval method is dependent only on the satellite based snow–ice interface
temperature. The snow–ice interface temperature used on a given day is taken from the nearest AMSR-E or AMSR2 grid cell
to the buoy location. The resultant sea ice thickness profiles and buoy profiles are plotted in Figure 2. It is clear from Figure 2
240 that the SLICE profiles agree well with the buoy sea ice thickness when initialized with an accurate initial ice thickness. The
correlation coefficients ranges from 0.965 to 0.999 with a mean of 0.991 and standard deviation of 0.01 across all buoys. The
bias, calculated by taking the mean over the entire profile length of the retrieval method result minus the buoy thickness, ranges
from -0.078 m to 0.132 m with a mean of 0.008 m and standard deviation of 0.059 m across the buoys. The bias grows with
time as the SLICE profile moves away from its initialized thickness.

245 The initial condition is very important for the accuracy of sea ice thickness SLICE retrieval method. At the same time, due
to the dependency of sea ice growth on initial thickness shown in Equation 7, an initial condition that is biased high will lead
to a lower growth rate and an initial thickness that is biased low will lead to a higher growth rate. In this way, SLICE is self
correcting. In Figure 3, the retrieval method is initialized with sea ice thickness that is 0.25 m both higher and lower than the
buoy thickness. The profiles follow the same smooth thermodynamic growth exhibited in Figure 2 and both approach the buoy
250 sea ice thickness over time.
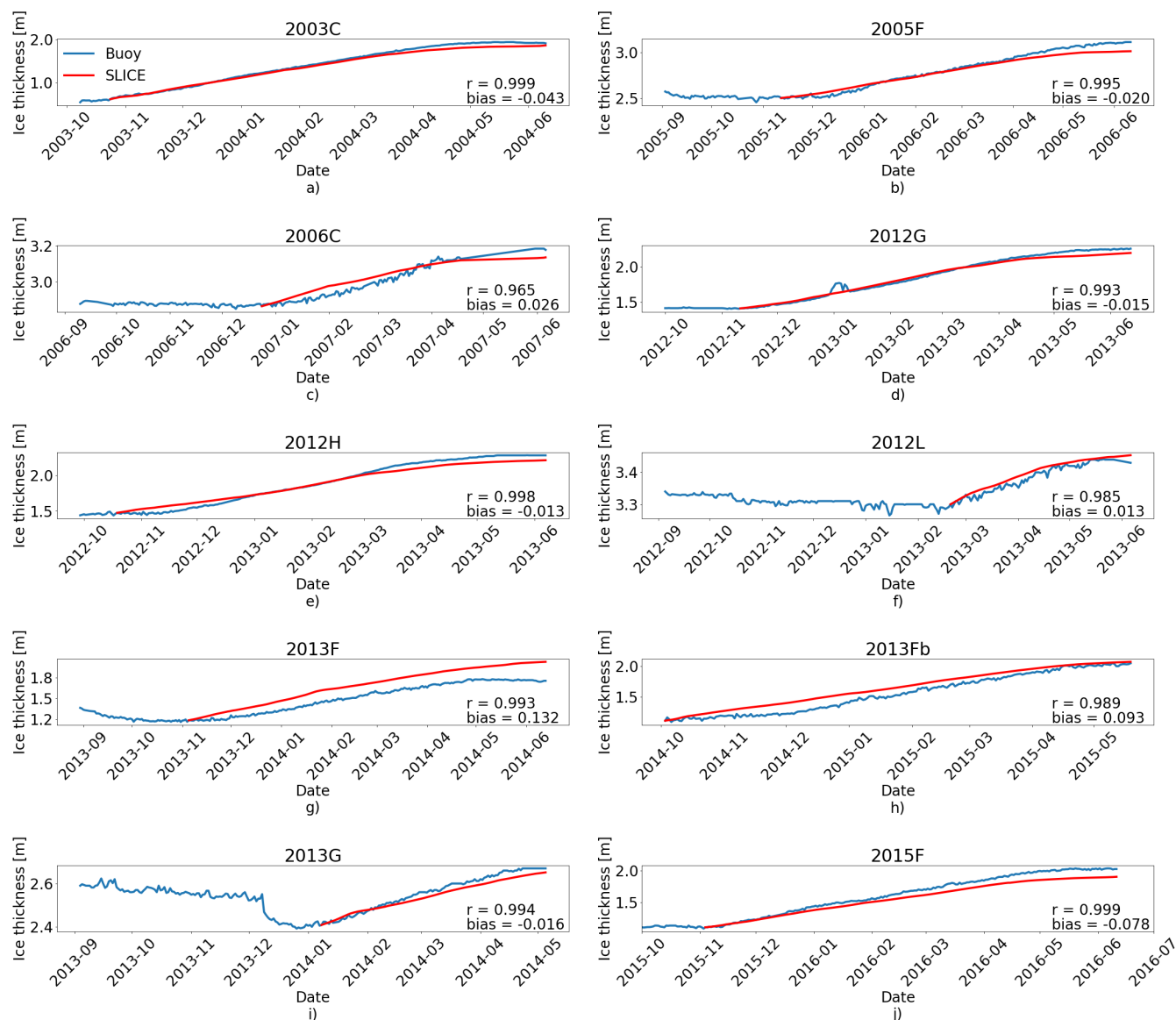
Figure 2. Ice thickness observations from ice mass balance buoys and SLICE for buoys (a) 2003C, (b) 2005F, (c) 2006C, (d) 2012G, (e) 2012H, (f) 2012L, (g) 2013F, (h) 2013Fb, (i) 2013G and (j) 2015F. Linear correlation (r) and bias values are listed. Across all buoys, the r values have a mean of 0.991 and the biases have a mean of 0.008 m.

4.2 Arctic Basin-wide Comparisons

Next, the SLICE retrieval method was applied on a Arctic basin-wide scale. Using the AWI CS2SMOS data for the first week of November as the initial state for one set of integration and the PIOMAS data from 1 November as the initial state for another
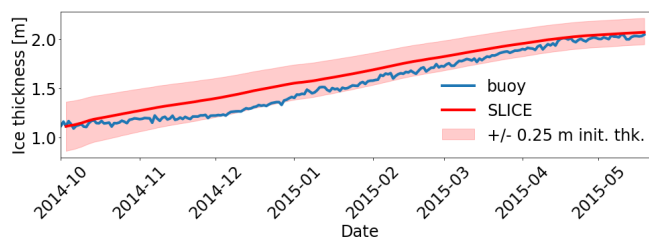
Figure 3. Ice thickness observations from ice mass balance buoys and sea ice thickness SLICE retrieval method for buoy 2013Fb with shading bounded by the retrieval method initialized at +/- 0.25 m. The higher and lower initialized profiles both approach the bold retrieval method profile with accurate initial condition over time.

set of integration, the retrieval method was applied daily to the entire Arctic basin from November to April for the growth
255   seasons beginning in 2012 through 2019. November first was chosen to ensure most ice was below the freezing point and there were limited melt ponds to interfere with the snow ice interface temperature observation. Only grid cells with 95% or greater sea ice concentration are considered, again to ensure accuracy of the snow ice interface temperature. The basin-wide results are on the 25km EASE-Grid 2.0. The AWI CS2SMOS data are on the same grid and the PIOMAS data are linearly interpolated from its native grid to the 25km EASE-Grid 2.0. The result is a daily gridded Arctic basin-wide sea ice thickness
260   dataset representing thermodynamic sea ice growth in the 95% sea ice concentration ice pack for the sea ice growth seasons beginning in the years 2012 to 2019. If at a given time step the AMSR-E and AMSR2 SIC product shows there is sea ice in a grid cell but the method does not, new ice is initialized at 0.05m. All ice motion is neglected in the creation of this dataset.

    Monthly basin-wide sea ice thickness plots for the sea ice growth season beginning in fall 2012 using AWI CS2SMOS as the initial state are shown in Figure 4. The sea ice thickness data from SLICE is available daily. The data from the first of every
265   month is plotted. The sea ice thickness on 30 April 2013 is higher but shows similar spatial distribution to that on 2 November 2012. The sea ice is growing thermodynamically but there is no dynamics to rearrange the thickness distribution.

    The cumulative effects of this lack of dynamics are depicted in Figures 5 and 6 which each compare sea ice thickness from SLICE to a reference dataset at the end of each growth season beginning in 2012 through 2019. Figure 5 compares SLICE to AWI CS2SMOS and Figure 6 compares SLICE with PIOMAS data. The end of the growth season is the week ending 15 April
270   for AWI CS2SMOS and 30 April for PIOMAS. The AWI CS2SMOS and PIOMAS data are a snapshot of the absolute thickness and would therefore capture both thermodynamic and dynamic processes. The differences are mostly between -1 m and 1 m and in most cases are near zero. The pattern exhibited by the differences is what would be expected from a lack of dynamic effects—lower SLICE sea ice thickness where anti-cyclonic flow pushes ice to the north of the Canadian Archipelago, lower SLICE sea ice thickness where the transpolar drift pushes ice to the east of Greenland and higher SLICE sea ice thickness
275   over the marginal seas from which the sea ice moves away after initial growth. Additionally, the SLICE retrieval method overestimates ice thickness in Baffin Bay in all years for both reference datasets, likely due to a lack of export of ice from this region.
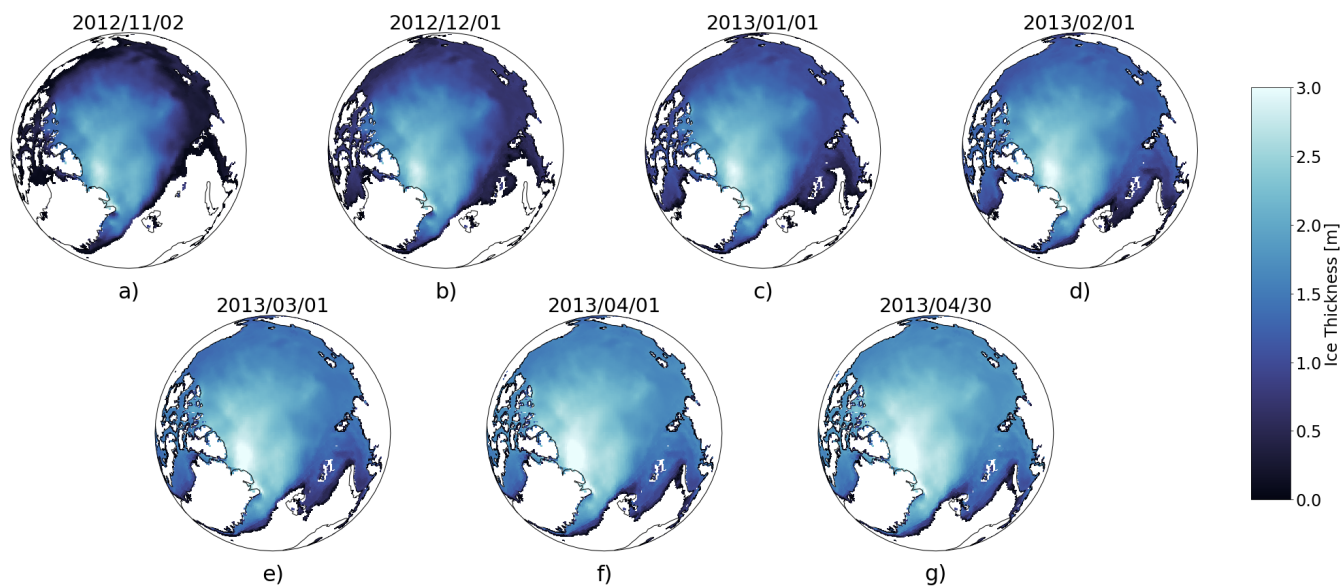
Figure 4. Sea ice thickness on a) 2 November 2012, b) 1 December 2012, c) 1 January 2013, d) 1 February 2012, d) 1 March 2013, e) 1 April 2013, f) 30 April 2013 created using SLICE with the November 1st, 2012 AWI CS2SMOS as an initial state. The overall structure changes little, as only thermodynamics are captured.

Tables 2 and 3 show the total yearly volumetric growth shown by the SLICE retrieval method and the AWI CS2SMOS and PIOMAS data respectively and their differences in absolute and relative terms. Only grid cells that contain ice in both
280 SLICE and the reference dataset were considered, likely meaning the marginal ice zone is excluded due to the retrieval method only capturing grid cells with >95% sea ice concentration. In all years, SLICE exceeds the volume growth captured by AWI CS2SMOS. Following the growth season beginning in 2013, SLICE only exceeded the AWI CS2SMOS volume growth by 4.2% of the AWI CS2SMOS growth but in most years SLICE exceeds the AWI CS2SMOS by over 10%. Following the growth season beginning in 2012, SLICE exceeds the AWI CS2SMOS volume growth by 18.1%. The SLICE retrieval method exceeds
285 AWI CS2SMOS in volumetric growth by a mean of 12.0% and a standard deviation of 5.5% in the years 2012–2019.

In contrast to in comparison with AWI CS2SMOS, the SLICE retrieval method underestimates volumetric sea ice growth in all years when compared to PIOMAS though the relative differences are reduced. SLICE produces a mean of 8.3% less volumetric growth compared to PIOMAS in the years 2012–2019. The differences are more consistent than in comparison with AWI CS2SMOS with a standard deviation of 2.0%. The maximum difference of 11.7% occurred following the growth
290 season beginning in 2017 and the minimum difference of 5.4% occurred following the growth season beginning in 2015. Again, only grid cells with ice in both datasets are considered.
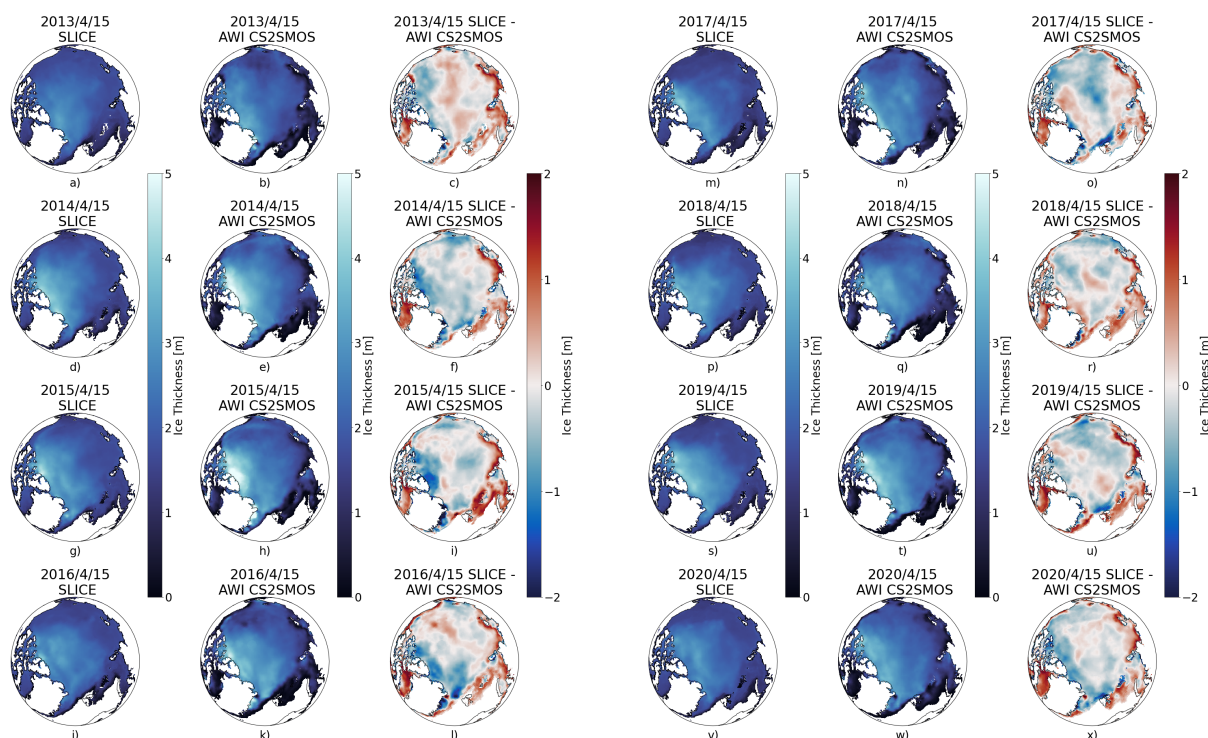
Figure 5. For the sea ice growth seasons ending in a–c) 2013, d–f) 2014, g–i) 2015, j–l) 2016, m–o) 2017, p–r) 2018, s–u) 2019 and v–x) 2020, SLICE initialized with AWI CS2SMOS from the first week of November, AWI CS2SMOS sea ice thickness and their difference on 15 April. Their differences represent dynamic changes and are in areas expected by climatology.

Table 2. A comparison of volumetric sea ice growth between AWI CS2SMOS and SLICE for the years 2021 through 2019. SLICE exceeds AWI CS2SMOS in volumetric growth by a mean of 12.0% and a standard deviation of 5.5%.

Winter Season	SLICE Volume Growth [km^3]	CS2SMOS Volume Growth [km^3]	Difference (SLICE - CS2SMOS) [km^3]	Difference/ CS2SMOS Volume Growth [%]
2012	13990	11849	2141	18.1
2013	11912	11433	478	4.2
2014	12479	11455	1024	8.9
2015	12102	10315	1787	17.3
2016	11962	11384	578	5.1
2017	11892	10386	1506	14.5
2018	12452	10677	1775	16.6
2019	13177	11790	1397	11.8
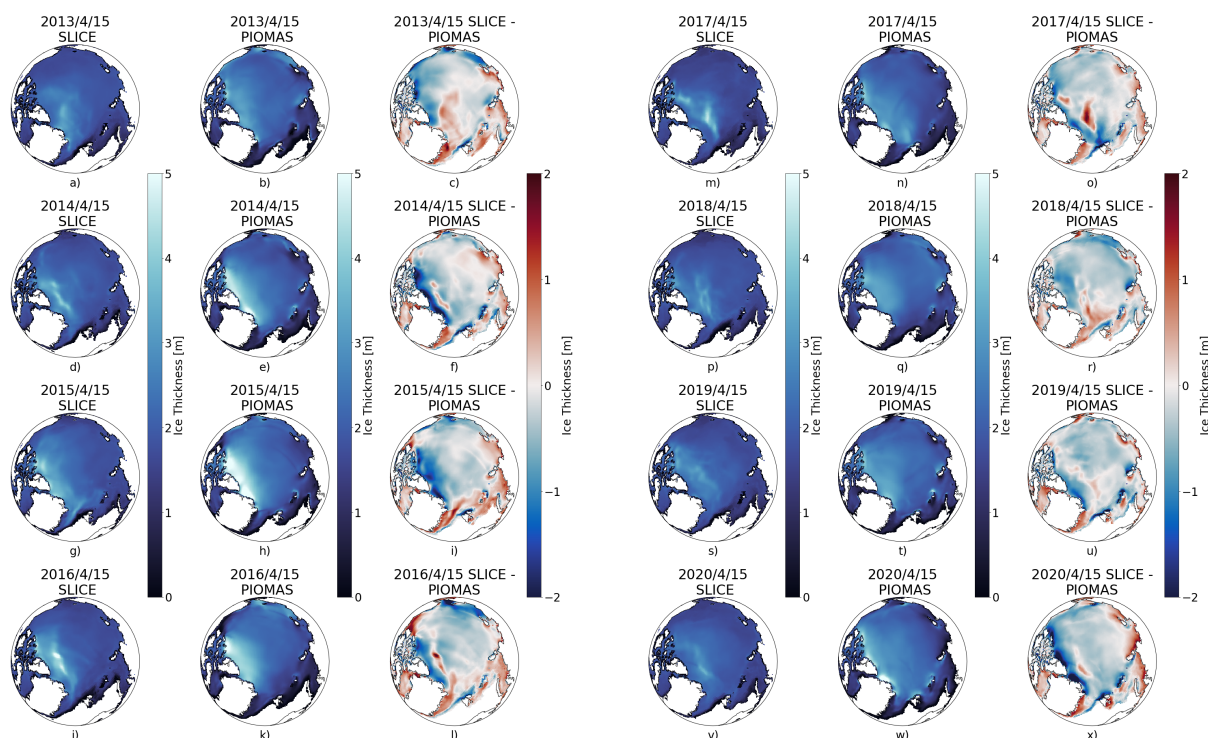
Figure 6. For the sea ice growth seasons ending in a–c) 2013, d–f) 2014, g–i) 2015, j–l) 2016, m–o) 2017, p–r) 2018, s–u) 2019 and v–x) 2020, SLICE initialized with PIOMAS on 1 November, PIOMAS sea ice thickness and their difference on 15 April. Their differences represent dynamic changes and are in areas expected by climatology.

Table 3. A comparison of volumetric sea ice growth between PIOMAS and SLICE for the years 2021 through 2020. PIOMAS exceeds SLICE in volumetric growth by a mean of 8.3% and a standard deviation of 2.0%.

Winter Season	SLICE Volume Growth [km^3]	PIOMAS Volume Growth [km^3]	Difference (SLICE - PIOMAS) [km^3]	Difference/ PIOMAS Volume Growth [%]
2012	14574	15862	-1287	-8.1
2013	12590	13738	-1148	-8.4
2014	12926	13870	-944	-6.8
2015	12518	13233	-715	-5.4
2016	12884	13811	-926	-6.7
2017	12556	14218	-1663	-11.7
2018	13225	14578	-1353	-9.3
2019	13867	15364	-1496	-9.7

5 Discussion

The SLICE retrieval method captures thermodynamic sea ice thickness accretion very well. Figure 2 shows a comparison between ice mass balance buoy sea ice thickness measurements and the retrieval method initialized with the buoy data for 10 buoys within the years 2003–2016. The mean correlation coefficient of 0.991 between the buoy measurements and the method is high. The bias values are also very encouraging with a mean of 0.008 m. Additionally, SLICE has a self-correcting quality by nature of Equation 7 whereby sea ice thicknesses that are biased in either direction approach the correct sea ice thickness over time as shown in Figure 3. These points suggest the retrieval method is viable as a basis for estimating sea ice thickness but is highly dependent on an initial condition, as it calculates thermodynamic sea ice thickness increase rather than absolute thickness.

While SLICE is capable of retrieving thermodynamic sea ice growth, it is unable to detect dynamic effects—i.e., thickness changes due to ice motion. Figure 4 shows monthly basin-wide plots of sea ice thickness for the sea ice growth season beginning on 1 November 2012 created using the retrieval method with an initial condition provided by the AWI CS2SMOS dataset. The sea ice thickness values are greater but the spatial distribution is similar from month to month as parcels are not moving, rather only growing thermodynamically. The consequences of this lack of dynamic sea ice thickness change are explored in Figures 5 and 6 showing basin-wide comparisons of sea ice thickness from SLICE to that from AWI CS2SMOS and PIOMAS, respectively. The AWI CS2SMOS and PIOMAS products both have thicker ice in regions where dynamic sea ice effects are expected to increase ice thickness, notably north of the Canadian Archipelago and east of Greenland, and thinner ice in the marginal seas from where ice is exported. The difference plots between SLICE and these reference datasets look similar in each year. These plots are integrated to a volume perspective in Tables 2 and 3. In all cases, SLICE is within 20% volumetric growth of the reference dataset. Interestingly, the retrieval method shows greater volumetric growth than CS2SMOS in all years and less volumetric growth than PIOMAS in all years.

These results are encouraging for the capability of SLICE to capture volumetric sea ice changes changes on a basin-wide scale. Per the model described by Equation 4, sea ice volume is only added through thermodynamic processes—dynamic processes only serve to rearrange the volume already present. Though this statement does invoke the false assumption that dynamic processes do not change the density of the ice, it seems to be a factor in explaining the volumetric results described in Tables 2 and 3. Though dynamic processes do not directly change sea ice volume, their changing of the thickness of ice at a given location does impact thermodynamic processes by virtue of f being a function of thickness, H, in Equation 4. Inspection of Equation 7 indeed shows that H impacts $\frac{\partial H}{\partial t}$. In regions where dynamic processes increase sea ice thickness, SLICE will overestimate sea ice thickness increase and in regions where dynamics decrease sea ice thickness, it will underestimate sea ice thickness increase. These phenomena, along with any phenomena inherent to either reference dataset, may explain volumetric differences between SLICE and the reference datasets.

Another potential factor explaining differences in volumetric growth of SLICE versus the reference datasets is the choice of sea ice growth start and end dates. Figure 2 shows that most buoys experience sea ice thickness growth beginning around 1 November. November first is also the start date for the basin-wide growth examples shown in Figures 4, 5 and 6 but this is

undoubtedly inaccurate for some of the Arctic basin, regions of which begin ice accretion at varying start dates based on local conditions. Additionally, SLICE is incapable of capturing ice melt. If at any time during the growth season a region were to experience melting, the associated ice thickness decrease would not be captured. SLICE results are dependent on the values provided for the freezing point of sea water, thermal conductivity, density and latent heat, all of which are not constant values

330   across the Arctic as we have treated them here. An additional value that is influential for the retrieval method is the initial 0.05 m ice given to grid cells where the SIC dataset shows new ice. A more rigorous treatment of these constants and their variation across the basin may improve the results.

There are a number of assumptions inherent to Stefan's Law (Lepparanta, 1993) that must be considered in relation to SLICE. In order to characterize conduction through the ice layer with only the snow–ice interface temperature and an assumed

335   freezing point temperature at the bottom of the ice layer, it must be assumed that heat conduction in the horizontal is negligible and that the local vertical derivative of temperature throughout the ice layer is constant. These assumptions are reasonable. The remaining two assumptions are more salient. The first is that there is no internal heat source. This is untrue when there is significant short wave radiation absorbed within the sea ice. The final assumption is that there is no heat exchange between the sea ice and the ocean, which is likely to be invalid in some regions. Another source of uncertainty in SLICE ice thickness

340   is the constraint that it is limited to areas with sea ice concentration greater than 95%. There is significant growth in areas where the sea ice concentration is low, such as the marginal ice zone (MIZ). This constraint would likely cause underestimated sea ice growth over those areas. In a supplement to the body of the paper, Lee and Sohn (2015) suggest a procedure for calculating snow–ice interface temperature in areas with less than 95% but that has not been implemented here, pending further investigation. Further validation of SLICE, particularly in regions other than the Beaufort Sea and Central Arctic, where all

345   ten buoys used here were located, as well as investigation of the impacts of these assumptions and full characterization of uncertainties is warranted.

The SLICE retrieval method uses passive microwave brightness temperatures from the AMSR-E and AMSR2 instruments and a snow–ice interface temperature retrieval algorithm (Lee and Sohn, 2015) to drive a sea ice thickness growth equation. Gridded brightness temperature data from these instruments are available at daily temporal resolution in the polar regions

350   (Cavalieri et al., 2014; Markus et al., 2018), meaning daily sea ice thickness growth is available basin-wide. Lee et al. (2018) provides a method for retrieving snow–ice interface temperatures using passive microwave brightness temperatures from the SSM/I and SSMIS instruments, allowing for the application of SLICE to sea ice growth seasons beginning in 1987. Current state of the art sea ice thickness observations from space, though capable of observing sea ice growth whether from thermo-dynamic or dynamic effects, are not capable of this spatial and temporal coverage. They also do not discriminate between

355   dynamic and thermodynamic effects. For these reasons, a sea ice thickness dataset based on SLICE will be especially qualified for investigating thermodynamic and dynamic sea ice phenomena that are small scale in space and time. SLICE need not be initialized the beginning of the growth season and applied for an entire growth season but can be initialized at any time during the growth season and applied to any interval of time, allowing for use with case studies or other small time and space scale events. Additionally, the high temporal resolution retrieval of thermodynamic effects will allow for creation of useful datasets

360   of surface energy flux from latent heat of fusion. Lastly, we are aware of no reason SLICE could not also be applied to Antarctic sea ice or freshwater bodies.

      With the availability of sea ice motion observation datasets from NSIDC (Tschudi et al., 2020) and the European Organisation for the Exploitation of Meteorological Satellites (EUMETSAT) Ocean and Sea Ice Satellite Application Facility (OSISAF) (Lavergne et al., 2010), there is potential to add a dynamic component to SLICE by solving the second term of Equation 4.

365   Much effort has gone into discretizing this term for use with numerical techniques. A discussion of solution schemes for this type of equation as it relates to sea ice transport is found in Lipscomb and Hunke (2004). An ideal scheme must conserve volume, must be stable, must be second-order accurate in space in order to avoid excessive diffusion, preserve monotonicity and be efficient. Early climate models utilized the multidimensional positive–definite advection transport algorithm (MPDATA) introduced in Smolarkiewicz (1984). The current iteration of the Los Alamos sea ice model (CICE) solves these types of trans-

370   port equations using an incremental remapping scheme (Hunke and Lipscomb, 2010; Lipscomb and Hunke, 2004). Numerical solution schemes such as these for solving the second term in Equation 4 are under consideration for use with this retrieval method but are beyond the scope of this present work. If a suitable dynamic component can be developed, a climatology of both thermodynamic and dynamic sea ice thickness growth will be created.

6   Conclusions

375   New methods for observing snow–ice interface temperature (Lee and Sohn, 2015) have made possible a new strategy for observing sea ice thickness from space during the winter growth season: Stefan's Law Integrated Conducted Energy (SLICE). The new strategy involves coupling observed satellite retrieved snow–ice interface temperature with Stefan's Law (Stefan, 1891; Lepparanta, 1993). In the Stefan's Law relationship, latent heat of fusion is conducted from the bottom of the ice layer where new ice forms to the snow–ice interface and this rate of conduction and accretion is calculated using the snow–ice

380   interface temperature and an assumed freezing point temperature at the bottom of the ice layer. An initial value is required as SLICE calculates sea ice thickness growth rather than absolute thickness and does not capture melting. Four assumptions make this relationship possible, including (1) negligible horizontal conduction, (2) no thermal inertia in the ice, (3) no internal heat sources and (4) no heat flux from the sea water.

      When SLICE is initialized with an ice mass balance buoy thickness and compared against that buoy's ice thickness profiles

385   during the ice growth season, the retrieval method compares extremely well with the buoy observed sea ice thickness growth. Using ten buoys from 2003 to 2016, the mean linear correlation value is 0.991 and the mean bias is 0.008 m. Two sets of basin-wide integrations were also performed for the winter growth seasons beginning in the years 2012–2020 using an initial state from the AWI CS2SMOS and PIOMAS datasets. SLICE underestimated volumetric growth in all years when compared to PIOMAS with a mean of 8.1% in relative difference and overestimated volumetric growth in all years when compared to

390   AWI CS2SMOS with a mean of 11.9% in relative difference. The differences between ice thickness estimated with SLICE, a thermodynamic method, and the reference data follow a pattern expected from the dynamic motion of the ice pack.

The SLICE retrieval method is only capable of retrieving thermodynamic sea ice growth, which neglects dynamic growth. While a better understanding of thermodynamic growth on its own is useful, a product that also includes dynamic growth would be advantageous to the field. With the availability of ice motion and ice drift satellite products, there is potential for a dynamics

395 component to be paired with the thermodynamic component demonstrated here. With the availability of snow–ice interface temperature beginning in 1987 and ice motion products beginning in 1978, a climatology of daily sea ice thickness, thermodynamic growth and dynamic growth on a basin-wide scale may be possible. Such a dynamic component and climatology are in development.

Data availability. Data shown in all figures is available upon request. Section 2 describes availability of datasets used in this analysis.

400 *Code and data availability.* Code used for the analysis presented here is available upon request.

Author contributions. All authors together conceived of the idea to use satellite retrieved snow–ice interface in a sea ice thickness satellite retrieval method. JA completed all analysis and wrote the first draft under guidance from YL and JK.

Competing interests. The authors declare that they have no conflict of interest.

Acknowledgements. This work was funded by the National Oceanic and Atmospheric Administration (NOAA) under grant no. NA20NES4320003.
405 The views, opinions, and findings contained in this report are those of the author(s) and should not be construed as an official National Oceanic and Atmospheric Administration or U.S. Government position, policy, or decision. The merging of CryoSat-2 und SMOS data was funded by the ESA project SMOS & CryoSat-2 Sea Ice Data Product Processing and Dissemination Service and data from November 1st, 2012 to April 15th, 2021 were obtained from https://www.meereisportal.de (grant: REKLIM-2013-04).

References

410 Bitz, C. M. and Roe, G. H.: A mechanism for the high rate of sea ice thinning in the Arctic Ocean, J. Climate, 17, 3623–3632, https://doi.org/10.1175/1520-0442(2004)017<3623:amfthr>2.0.co;2, 2004.

Cavalieri, D. J., Gloersen, P., and Campbell, W. J.: Determination of sea ice parameters with the Nimbus-7 SMMR, J. Geophys. Res.-Atmos., 89, 5355–5369, https://doi.org/10.1029/JD089iD04p05355, 1984.

Cavalieri, D. J., Markus, T., and Comiso, J. C.: AMSR-E/Aqua Daily L3 25 km Brightness Temperature & Sea Ice Concentration Polar
415 Grids, Version 3, Boulder, Colorado USA. NASA National Snow and Ice Data Center Distributed Active Archive Center [data set], https://doi.org/https://doi.org/10.5067/AMSR-E/AE_SI25.003, 2014.

Comiso, J. C.: Sea ice effective microwave emissivities from satellite passive microwave and infrared observations, J. Geophys. Res.-Oceans, 88, 7686–7704, https://doi.org/10.1029/JC088iC12p07686, 1983.

Comiso, J. C.: Enhanced Sea Ice Concentrations and Ice Extents from AMSR-E Data, Journal of The Remote Sensing Society of Japan, 29,
420 199–215, https://doi.org/10.11440/rssj.29.199, 2009.

Connor, L. N., Laxon, S. W., Ridout, A. L., Krabill, W. B., and McAdoo, D. C.: Comparison of Envisat radar and airborne laser altimeter measurements over Arctic sea ice, Remote Sens. Environ., 113, 563–570, https://doi.org/10.1016/j.rse.2008.10.015, 2009.

Docquier, D. and Koenigk, T.: Observation-based selection of climate models projects Arctic ice-free summers around 2035, Nature Communications Earth & Environment, 2, 144, https://doi.org/10.1038/s43247-021-00214-7, 2021.

425 Gloersen, P. and Cavalieri, D. J.: Reduction of weather effects in the calculation of sea ice concentration from microwave radiances, J. Geophys. Res.-Oceans, 91, 3913–3919, https://doi.org/10.1029/JC091iC03p03913, 1986.

Guerreiro, K., Fleury, S., Zakharova, E., Kouraev, A., Remy, F., and Maisongrande, P.: Comparison of CryoSat-2 and ENVISAT radar freeboard over Arctic sea ice: toward an improved Envisat freeboard retrieval, Cryosphere, 11, 2059–2073, https://doi.org/10.5194/tc-11-2059-2017, 2017.

430 Hall, D. K., Key, J. R., Casey, K. A., Riggs, G. A., and Cavalieri, D. J.: Sea ice surface temperature product from MODIS, IEEE T. Geosci. Remote., 42, 1076–1087, https://doi.org/10.1109/tgrs.2004.825587, 2004.

Hendricks, S. and Ricker, R.: Product User Guide & Algorithm Specification: AWI CryoSat-2 Sea Ice Thickness (version 2.3), https://doi.org/10013/epic.ecd56b5d-3e7d-4a65-9019-588b1c3b0d26, 2020.

Hendricks, S., Paul, S., and Rinne, E.: ESA Sea Ice Climate Change Initiative (Sea_Ice_cci): Northern hemisphere sea
435 ice thickness from the CryoSat-2 satellite on a monthly grid (L3C), v2.0. Centre for Environmental Data Analysis, https://doi.org/10.5285/ff79d140824f42dd92b204b4f1e9e7c2, 2018.

Hewison, T. J. and English, S. J.: Airborne retrievals of snow and ice surface emissivity at millimeter wavelengths, IEEE T. Geosci. Remote., 37, 1871–1879, https://doi.org/10.1109/36.774700, 1999.

Hibler, W. D.: Dynamic Thermodynamic Sea Ice Model, J Phys. Oceanogr., 9, 815–846, https://doi.org/10.1175/1520-
440 0485(1979)009<0815:adtsim>2.0.co;2, 1979.

Hunke, E. and Lipscomb, H.: CICE: the Los Alamos Sea Ice Model Documentation and Software User's Manual, Version 4.1, LA-CC-06-012, https://doi.org/https://csdms.colorado.edu/w/images/CICE_documentation_and_software_user%27s_manual.pdf (last access: 27 August 2021), 2010.

Kang, E. J., Sohn, B. J., Tonboe, R. T., Dybkjaer, G., Holmlund, K., Kim, J. M., and Liu, C.: Implementation of a 1-D Thermodynamic
     Model for Simulating the Winter-Time Evolvement of Physical Properties of Snow and Ice Over the Arctic Ocean, J. Adv. Model. Earth
     Sy., 13, 3, https://doi.org/10.1029/2020ms002448, 2021.

Key, J., Wang, X. J., Liu, Y. H., Dworak, R., and Letterly, A.: The AVHRR Polar Pathfinder Climate Data Records, Remote Sensing, 8, 3,
     https://doi.org/10.3390/rs8030167, 2016.

Kilic, L., Tonboe, R. T., Prigent, C., and Heygster, G.: Estimating the snow depth, the snow–ice interface temperature, and the effective
     temperature of Arctic sea ice using Advanced Microwave Scanning Radiometer 2 and ice mass balance buoy data, Cryosphere, 13, 1283–
     1296, https://doi.org/10.5194/tc-13-1283-2019, 2019.

Kurtz, N. T., Galin, N., and Studinger, M.: An improved CryoSat-2 sea ice freeboard retrieval algorithm through the use of waveform fitting,
     Cryosphere, 8, 1217–1237, https://doi.org/10.5194/tc-8-1217-2014, 2014.

Kwok, R. and Cunningham, G. F.: ICESat over Arctic sea ice: Estimation of snow depth and ice thickness, J. Geophys. Res.-Oceans, 113,
     C08 010, https://doi.org/10.1029/2008jc004753, 2008.

Kwok, R. and Cunningham, G. F.: Variability of Arctic sea ice thickness and volume from CryoSat-2, Philos. T. Roy. Soc. A, 373, 2045,
     https://doi.org/10.1098/rsta.2014.0157, 2015.

Lavergne, T., Eastwood, S., Teffah, Z., Schyberg, H., and Breivik, L. A.: Sea ice motion from low-resolution satellite sensors: An alternative
     method and its validation in the Arctic, J. Geophys. Res.-Oceans, 115, C10 032, https://doi.org/10.1029/2009jc005958, 2010.

Lavergne, T., Surensen, A. M., Kern, S., Tonboe, R., Notz, D., Aaboe, S., Bell, L., Dybkjaer, G., Eastwood, S., Gabarro, C., Heygster, G.,
     Killie, M. A., Kreiner, M. B., Lavelle, J., Saldo, R., Sandven, S., and Pedersen, L. T.: Version 2 of the EUMETSAT OSI SAF and ESA
     CCI sea-ice concentration climate data records, Cryosphere, 13, 49–78, https://doi.org/10.5194/tc-13-49-2019, 2019.

Laxon, S. W., Giles, K. A., Ridout, A. L., Wingham, D. J., Willatt, R., Cullen, R., Kwok, R., Schweiger, A., Zhang, J. L., Haas, C., Hendricks,
     S., Krishfield, R., Kurtz, N., Farrell, S., and Davidson, M.: CryoSat-2 estimates of Arctic sea ice thickness and volume, Geophys. Res.
     Lett., 40, 732–737, https://doi.org/10.1002/grl.50193, 2013.

Lee, S. M. and Sohn, B. J.: Retrieving the refractive index, emissivity, and surface temperature of polar sea ice from 6.9GHz microwave
     measurements: A theoretical development, J. Geophys. Res.-Atmos., 120, 2293–2305, https://doi.org/10.1002/2014jd022481, 2015.

Lee, S. M., Sohn, B. J., and Kummerow, C. D.: Long-Term Arctic Snow/Ice Interface Temperature from Special Sensor for Microwave
     Imager Measurements, Remote Sensing, 10, 11, https://doi.org/10.3390/rs10111795, 2018.

Lepparanta, M.: A Review of Analytical Models of Sea–Ice Growth, Atmos. Ocean, 31, 123–138,
     https://doi.org/10.1080/07055900.1993.9649465, 1993.

Lipscomb, W. H. and Hunke, E. C.: Modeling sea ice transport using incremental remapping, Mon. Weather Rev., 132, 1341–1354,
     https://doi.org/10.1175/1520-0493(2004)132<1341:msitui>2.0.co;2, 2004.

Liu, Y. H., Key, J. R., and Wang, X. J.: Influence of changes in sea ice concentration and cloud cover on recent Arctic surface temperature
     trends, Geophys. Res. Lett., 36, L20 710, https://doi.org/10.1029/2009gl040708, 2009.

Liu, Y. H., Key, J., and Mahoney, R.: Sea and Freshwater Ice Concentration from VIIRS on Suomi NPP and the Future JPSS Satellites,
     Remote Sensing, 8, 6, https://doi.org/10.3390/rs8060523, 2016.

Liu, Y. H., Key, J. R., Wang, X. J., and Tschudi, M.: Multidecadal Arctic sea ice thickness and volume derived from ice age, Cryosphere, 14,
     1325–1345, https://doi.org/10.5194/tc-14-1325-2020, 2020.

Markus, T. and Cavalieri, D. J.: An enhancement of the NASA Team sea ice algorithm, IEEE T. Geosci. Remote., 38, 1387–1398,
     https://doi.org/10.1109/36.843033, 2000.

Markus, T. and Cavalieri, D. J.: The AMSR-E NT2 Sea Ice Concentration Algorithm : its Basis and Implementation, Journal of The Remote Sensing Society of Japan, 29, 216–225, https://doi.org/10.11440/rssj.29.216, 2009.

Markus, T., Neumann, T., Martino, A., Abdalati, W., Brunt, K., Csatho, B., Farrell, S., Fricker, H., Gardner, A., Harding, D., Jasinski, M., Kwok, R., Magruder, L., Lubin, D., Luthcke, S., Morison, J., Nelson, R., Neuenschwander, A., Palm, S., Popescu, S., Shum, C. K., Schutz, B. E., Smith, B., Yang, Y. K., and Zwally, J.: The Ice, Cloud, and land Elevation Satellite-2 (ICESat-2): Science requirements, concept, and implementation, Remote Sens. Environ., 190, 260–273, https://doi.org/10.1016/j.rse.2016.12.029, 2017.

Markus, T., Comiso, J. C., and Meier, W. N.: AMSR-E/AMSR2 Unified L3 Daily 25 km Brightness Temperatures & Sea Ice Concentration Polar Grids, Version 1, Boulder, Colorado USA. NASA National Snow and Ice Data Center Distributed Active Archive Center [data set], https://doi.org/https://doi.org/10.5067/TRUIAL3WPAUP, 2018.

Massonnet, F., Vancoppenolle, M., Goosse, H., Docquier, D., Fichefet, T., and Blanchard-Wrigglesworth, E.: Arctic sea–ice change tied to its mean state through thermodynamic processes, Nat. Clim. Change, 8, 599–603, https://doi.org/10.1038/s41558-018-0204-z, 2018.

Mathew, N., Heygster, G., and Melsheimer, C.: Surface Emissivity of the Arctic Sea Ice at AMSR-E Frequencies, IEEE T. Geosci. Remote., 47, 4115–4124, https://doi.org/10.1109/tgrs.2009.2023667, 2009.

Mayer, M., Tietsche, S., Haimberger, L., Tsubouchi, T., Mayer, J., and Zuo, H.: An Improved Estimate of the Coupled Arctic Energy Budget, J. Climate, 32, 7915–7934, https://doi.org/10.1175/jcli-d-19-0233.1, 2019.

Mecklenburg, S., Drusch, M., Kerr, Y. H., Font, J., Martin-Neira, M., Delwart, S., Buenadicha, G., Reul, N., Daganzo-Eusebio, E., Oliva, R., and Crapolicchio, R.: ESA's Soil Moisture and Ocean Salinity Mission: Mission Performance and Operations, IEEE T. Geosci. Remote., 50, 1354–1366, https://doi.org/10.1109/tgrs.2012.2187666, 2012.

Meier, W. N., Stewart, J. S., Liu, Y. H., Key, J., and Miller, J. A.: Operational Implementation of Sea Ice Concentration Estimates From the AMSR2 Sensor, IEEE J. Sel. Top. Appl., 10, 3904–3911, https://doi.org/10.1109/jstars.2017.2693120, 2017.

Perovich, D., Richter-Menge, J., and Polashenski, C.: Observing and understanding climate change: Monitoring the mass balance, motion, and thickness of Arctic sea ice, http://imb-crrel-dartmouth.org, 2021.

Polashenski, C., Perovich, D., Richter-Menge, J., and Elder, B.: Seasonal ice mass-balance buoys: adapting tools to the changing Arctic, Ann. Glaciol., 52, 18–26, https://doi.org/10.3189/172756411795931516, 2011.

Richter-Menge, J. A., Perovich, D. K., Elder, B. C., Claffey, K., Rigor, I., and Ortmeyer, M.: Ice mass–balance buoys: a tool for measuring and attributing changes in the thickness of the Arctic sea–ice cover, Ann. Glaciol., 44, 205–210, https://doi.org/10.3189/172756406781811727, 2006.

Ricker, R., Hendricks, S., Helm, V., Skourup, H., and Davidson, M.: Sensitivity of CryoSat-2 Arctic sea–ice freeboard and thickness on radar-waveform interpretation, Cryosphere, 8, 1607–1622, https://doi.org/10.5194/tc-8-1607-2014, 2014.

Ricker, R., Hendricks, S., Kaleschke, L., and Tian-Kunze, X.: CS2SMOS User Guide v3.0, https://doi.org/10013/epic.51136, 2017a.

Ricker, R., Hendricks, S., Kaleschke, L., Tian-Kunze, X., King, J., and Haas, C.: A weekly Arctic sea-ice thickness data record from merged CryoSat-2 and SMOS satellite data, Cryosphere, 11, 1607–1623, https://doi.org/10.5194/tc-11-1607-2017, 2017b.

Sallila, H., Farrell, S. L., McCurry, J., and Rinne, E.: Assessment of contemporary satellite sea ice thickness products for Arctic sea ice, Cryosphere, 13, 1187–1213, https://doi.org/10.5194/tc-13-1187-2019, 2019.

Schweiger, A., Lindsay, R., Zhang, J. L., Steele, M., Stern, H., and Kwok, R.: Uncertainty in modeled Arctic sea ice volume, J. Geophys. Res.-Oceans, 116, C00D06, https://doi.org/10.1029/2011jc007084, 2011.

Screen, J. A. and Simmonds, I.: The central role of diminishing sea ice in recent Arctic temperature amplification, Nature, 464, 1334–1337, https://doi.org/10.1038/nature09051, 2010.

520 Smolarkiewicz, P. K.: A fully multidimensional positive definite advection transport algorithm with small implicit diffusion, J. Comput. Phys., 54, 325–362, https://doi.org/10.1016/0021-9991(84)90121-9, 1984.

Sohn, B. J. and Lee, S. M.: Analytical relationship between polarized reflectivities on the specular surface, Int. J. Remote Sens., 34, 2368–2374, https://doi.org/10.1080/01431161.2012.744490, 2013.

Stefan, J.: Ueber die Theorie der Eisbildung, insbesondere über die Eisbildung im Polarmeere, Ann. der Phy.-Berlin, 278, 269–286,
525 https://doi.org/https://doi.org/10.1002/andp.18912780206, 1891.

Stroeve, J. C., Serreze, M. C., Holland, M. M., Kay, J. E., Malanik, J., and Barrett, A. P.: The Arctic's rapidly shrinking sea ice cover: a research synthesis, Climatic Change, 110, 1005–1027, https://doi.org/10.1007/s10584-011-0101-1, 2012.

Thorndike, A. S., Rothrock, D. A., Maykut, G. A., and Colony, R.: Thickness Distribution of Sea Ice, J. Geophys. Res.-Oc. Atm., 80, 4501–4513, https://doi.org/10.1029/JC080i033p04501, 1975.

530 Tian-Kunze, X., Kaleschke, L., Maass, N., Makynen, M., Serra, N., Drusch, M., and Krumpen, T.: SMOS-derived thin sea ice thickness: algorithm baseline, product specifications and initial verification, Cryosphere, 8, 997–1018, https://doi.org/10.5194/tc-8-997-2014, 2014.

Tilling, R. L., Ridout, A., and Shepherd, A.: Estimating Arctic sea ice thickness and volume using CryoSat-2 radar altimeter data, Adv. Space Res., 62, 1203–1225, https://doi.org/10.1016/j.asr.2017.10.051, 2018.

Tschudi, M. A., Meier, W. N., and Stewart, J. S.: An enhancement to sea ice motion and age products at the National Snow and Ice Data
535 Center (NSIDC), Cryosphere, 14, 1519–1536, https://doi.org/10.5194/tc-14-1519-2020, 2020.

Wang, X. J., Key, J., Kwok, R., and Zhang, J. L.: Comparison of Arctic Sea Ice Thickness from Satellites, Aircraft, and PIOMAS Data, Remote Sensing, 8, 9, https://doi.org/10.3390/rs8090713, 2016.

Wingham, D. J., Francis, C. R., Baker, S., Bouzinac, C., Brockley, D., Cullen, R., de Chateau-Thierry, P., Laxon, S. W., Mallow, U., Mavrocordatos, C., Phalippou, L., Ratier, G., Rey, L., Rostan, F., Viau, P., and Wallis, D. W.: CryoSat: A mission to determine the
540 fluctuations in Earth's land and marine ice fields, Natural Hazards and Oceanographic Processes from Satellite Data, 37, 841–871, https://doi.org/10.1016/j.asr.2005.07.027, 2006.

Zhang, J. L. and Rothrock, D. A.: Modeling global sea ice with a thickness and enthalpy distribution model in generalized curvilinear coordinates, Mon. Weather Rev., 131, 845–861, https://doi.org/10.1175/1520-0493(2003)131<0845:mgsiwa>2.0.co;2, 2003.